



**HAL**  
open science

## **An impedimetric immunosensor based on PAMAM decorated electrospun polystyrene fibers for detection of interleukin-10 cytokine**

Pouyan Razmshoar, S. Hajir Bahrami, Mohammad Rabiee, Isaac A.M. Frias, Marie Hangouet, Marie Martin, François Bessueille, Abdelhamid Errachid, Nicole Jaffrezic-Renault

### ► To cite this version:

Pouyan Razmshoar, S. Hajir Bahrami, Mohammad Rabiee, Isaac A.M. Frias, Marie Hangouet, et al.. An impedimetric immunosensor based on PAMAM decorated electrospun polystyrene fibers for detection of interleukin-10 cytokine. *Journal of Electroanalytical Chemistry*, 2022, 926, pp.116953. 10.1016/j.jelechem.2022.116953 . hal-03996688

**HAL Id: hal-03996688**

**<https://hal.science/hal-03996688v1>**

Submitted on 20 Feb 2023

**HAL** is a multi-disciplinary open access archive for the deposit and dissemination of scientific research documents, whether they are published or not. The documents may come from teaching and research institutions in France or abroad, or from public or private research centers.

L'archive ouverte pluridisciplinaire **HAL**, est destinée au dépôt et à la diffusion de documents scientifiques de niveau recherche, publiés ou non, émanant des établissements d'enseignement et de recherche français ou étrangers, des laboratoires publics ou privés.

# An impedimetric immunosensor based on PAMAM decorated electrospun polystyrene fibers for detection of interleukin-10 cytokine

Pouyan Razmshoar<sup>1</sup>, S. Hajir Bahrami<sup>1\*</sup>, Mohammad Rabiee<sup>2</sup>, Isaac A.M. Frias<sup>3</sup>, Marie Hangouet<sup>3</sup>,  
Marie Martin<sup>3</sup>, François Bessueille<sup>3</sup>, Abdelhamid Errachid<sup>3</sup>, Nicole Jaffrezic-Renault<sup>3\*</sup>

1. Textile Engineering Department, Amirkabir University of Technology (Tehran Polytechnic), Tehran,  
Iran

2. Biomedical Engineering Department, Amirkabir University of Technology (Tehran Polytechnic),  
Tehran, Iran

3. University of Lyon, Institute of Analytical Sciences, UMR 5280, CNRS, F-69100, Villeurbanne,  
France

Corresponding authors: S. Hajir Bahrami, hajirb@aut.ac.ir ; Nicole Jaffrezic-Renault,  
nicole.jaffrezic@univ-lyon1.fr

## Abstract:

Cytokine storms are known as the uncontrolled overproduction of inflammatory cytokines that can be produced by a variety of viral or non-infectious disorders and inflict significant damage to many organs. Interleukin-10 (IL-10) is an anti-inflammatory cytokine, and rapid detection of its levels in serum and saliva is important for many diseases, including severe COVID-19 patients. In this study, Polystyrene (PS) fibers were electrospun over a gold electrode and modified by air plasma to allow their further decoration with polyamidoamine (PAMAM) dendritic polymer for providing many active sites on the fiber surface. The fabricated three-dimensional (3-D) architecture was employed as a platform in an impedimetric immunosensor for the quantitative detection of interleukin-10 cytokine (AgIL-10). Scanning electron microscopy (SEM), Fourier transform infrared spectroscopy (FTIR), contact angle measurements, fluorescence microscopy, UV-vis spectroscopy, and electrochemical methods including cyclic voltammetry (CV) and electrochemical impedance spectroscopy (EIS) were used to characterize the proposed electrospun fiber-based platform and electrochemical immunosensor. The PAMAM properties increased not only the amperometric response to the ferro/ferri cyanide redox probe, of the modified gold

29 electrode but also the active surface area available for covalently binding of anti-IL-10 capture antibody,  
30 resulting in the sensitive detection of AgIL-10 in the concentration range of (1-50 pg/mL) in phosphate  
31 buffer saline (PBS) with a limit of detection (LOD) of 1 pg/mL. The immunosensor's performance in  
32 detecting AgIL-10 in artificial saliva (AS) as a complex medium was likewise satisfactory. This  
33 immunosensor provides a new opportunity for clinical immunoassays thanks to its great  
34 sensitivity, selectivity, and stability.

35 **Keywords:** Immunosensor, Fibers, Plasma, Polystyrene, Polyamidoamine (PAMAM), Interleukin-10

## 36 1. Introduction

37 Cytokine storms are defined as excessively high and exaggerated cytokine production originating from a  
38 variety of viral and non-infectious disorders, causing severe inflammatory responses and organ damage. [1]  
39 Interleukin-10 (IL-10) is an anti-inflammatory cytokine produced by T helper 2 cells that plays an important  
40 role in immunoregulation and inflammation management. [2,3] IL-10 has been considered as a viable  
41 therapeutic and diagnostic tool for a variety of diseases, including inflammatory autoimmune diseases. [4,5]  
42 Recent studies with coronavirus (COVID-19) patients' non-survivors have reported elevated concentrations  
43 of interleukin-6 (IL-6) and IL-10 cytokines compared with survivors owing to hyperinflammation [6–8].  
44 The findings from 102 COVID-19 patients reveal that the median level of IL-10 cytokine in their serum,  
45 (5.37 pg/mL) was 37% higher than the median level in healthy serum (3.91 pg/mL) [1]. Salivary IL-10  
46 cytokine levels in COVID-19 and post-COVID-19 patients have been reported to be  $10.01 \pm 2.05$  pg/mL  
47 and  $9.08 \pm 1.17$  pg/mL, respectively. These findings suggest that elevated IL-10 concentrations could be  
48 utilized to predict the severity of COVID-19 [9].

49 The enzyme-linked immunosorbent assay (ELISA) is regularly used as a standard laboratory test for  
50 cytokine detection. Despite its great sensitivity and precision, this approach is expensive, time-consuming,  
51 and requires the analysis of professional specialists. [10,11] Hence, more accessible, highly sensitive, and  
52 selective diagnostic methods for the detection of inflammatory cytokines are urgently needed to enable

53 early therapeutic intervention and improve patient quality of life. [12] Electrochemical immunosensors, as  
54 opposed to these suggested techniques, have attracted a lot of interest because of their significant features,  
55 such as ease of use, swiftness, portability, time and cost effectiveness, and excellent sensitivity. [13] These  
56 immunological responses triggered by particular probe-target complexes are characterized by legible  
57 current signals. The signal amplification strategy is the most widespread and effective way for increasing  
58 the sensitivity of electrochemical immunosensors. In this regard, several approaches can be followed to  
59 improve the electron transport efficiency and surface area of the substrate while keeping the immunological  
60 molecule's activity. [14] Multiple nanomaterials have been employed in the creation of electrochemical  
61 immunosensors and improve their performance as a result of the quick development of nanomaterial  
62 breakthroughs due to their numerous benefits, including high stability, strong electrocatalytic activity, and  
63 ease of modification. [15–17]

64 The ability to electrospun fibers (ESFs) mats with a high surface area, mechanical flexibility, good surface  
65 functionalization, and interconnected porosity, which helps in the stabilization of higher receptors with  
66 better contact with the surrounding medium and access to the target analyte, underpins their use in the  
67 production of 3-D interfaces for electrochemical nano-biosensors. [18–21] Among the various fiber-  
68 forming technologies, electrospinning is known as an efficient, low-cost, simple, and versatile tool which  
69 uses electrostatic forces to generate polymer nanofibers (NFs) of different morphologies and diameters  
70 from solutions, suspensions, or melts[20]. Normally, in the electrospinning synthesis of NFs, the solution  
71 is extruded at a constant feed rate through the capillary to the tip of the spinneret, resulting in a pendant  
72 liquid drop due to surface tension. When an electric field is applied, electrostatic repulsion of surface  
73 charges of the same sign on the polymer droplet occurs, causing it to deform into a cone shape (known as  
74 a Taylor cone). By increasing the electric field and the dominance of electric force over surface tension, a  
75 charged polymer jet emerges from the cone, undergoing stretching, elongation, solvent evaporation, and  
76 solidification in the distance between the nozzle and the collector. [20,22,23]

77 Our major objective in this project was to create a new ESF-based transducer for the detection of AgIL-10  
78 by directly electrospinning PS ESFs on the surface of a gold electrode. PS was chosen as a polymer for its  
79 high mechanical characteristics, great shape stability in aqueous media without swelling, and low cost. [24]  
80 However, PS alone cannot offer an ideal interface because it lacks the surface-active groups and sufficient  
81 hydrophilicity needed for biological recognition elements' covalent attachment. [19] For this reason, plasma  
82 treatment, a process that alters the surface of polymers, increase their surface energy, and their  
83 hydrophilicity while maintaining their advantageous bulk features intact [25,26], was utilized to produce  
84 carboxyl groups on the PS fiber surface before decorating the fibers with the second generation (G2) of  
85 PAMAM dendritic polymer. PAMAM dendrimers with huge peripheral groups have been employed as  
86 branching polymeric macromolecules in the construction of different biosensors to readily interact with a  
87 large variety of bioreceptors, boosting their sensitivity, and improving their detection limit. [27,28] Grafting  
88 highly branched PAMAM polymer onto the fiber's surface can overcome the drawbacks of PS fibers, such  
89 as their hydrophobicity and lack of functional groups. Furthermore, the synergistic properties of electrospun  
90 fibers and highly branched polymers to create immunosensors with high capture antibody immobilization  
91 and increased sensitivity would be beneficial.

92 In a previous report, our group employed electrospinning to create a composite nanofiber from PS and  
93 PAMAM dendritic polymers in a one-step process by blending their solutions and using it as a 3-D interface  
94 to detect TNF-alpha cytokines. [29] As novelty, the benefit of decorating PAMAM on the PS fiber surface  
95 avails higher accessibility to PAMAM amine groups due to their larger loading on the fiber surface at  
96 considerably lower PAMAM concentrations. To create a strong covalent bond between the anti-IL-10 and  
97 the fiber surface, glutaraldehyde coupling chemistry was used to create a bond between the PAMAM  
98 dendritic polymer groups and the amine groups in the Fc region of the anti-IL-10. Schematic 1 depicts all  
99 stages of the immunosensor fabrication. Cyclic voltammetry (CV) and electrochemical impedance  
100 spectroscopy (EIS) were used to characterize the electrochemical characteristics of the developed ESFs-  
101 based immunosensor at each stage and AgIL-10 impedimetric detection, respectively.

102 Schematic.1.

## 103 **2. Experimental**

### 104 *2.1. Chemicals and reagents*

105 The reagents, instruments, and characterizations sections were thoroughly discussed in the supplementary  
106 information.

### 107 *2.2. Immunosensor preparation*

#### 108 *2.2.1. Preparation of PS ESFs*

109 PS granules were dissolved in DMF and stirred overnight to make a 25 wt.% electrospinning solution. A  
110 vertical electrospinning setup (Spraybase®, Ireland) was used for producing ESFs, which included a  
111 polytetrafluoroethylene (PTFE) tube to transfer the polymer solution from the pump to the nozzle. The  
112 electrospinning parameters, including voltage, feed rates, and nozzle to collector distance, were set at 27  
113 kV, 0.25 mL/h, and 20 cm, respectively, with these parameters having been previously optimized. [19] To  
114 achieve the highest level of similarity between the electrodes in terms of the thickness and amount of ESFs  
115 deposited, fibers were electrospun on gold electrodes for 1 min each by placing each on a specific location  
116 of aluminum foil. Before electrospinning, the gold electrodes were cleaned in an ultrasonic bath for 15 min  
117 in an acetone solution and then in an ethanol solution and were rinsed with ultrapure water at each stage  
118 and at the end. Then they were dried with a mild stream of nitrogen (N<sub>2</sub>) and then placed in a UV-ozone  
119 ProCleaner™ for 30 min to eliminate any possible organic contamination. This process results in a gold  
120 electrode with a hydrophilic feature, which increases not only fiber adherence to the electrode surface but  
121 also electrode wettability and electron transfer. Then the electrodes containing ESFs were stored at room  
122 temperature (RT) for subsequent use.

#### 123 *2.2.2. Air plasma treatment*

124 Gold electrodes modified with ESFs were treated with a frequency/low pressure (13.56 MHz, 50 W) plasma  
125 generator (Pico PCCE, Diener Electronic, Ebhausen, Germany) to produce carboxylic acid groups on the  
126 surface of the PS ESFs. By the time the electrodes were placed in the center of the chamber, the pressure  
127 within the chamber was reduced to 0.2 mbar by pumping to remove the air. The chamber was then filled  
128 with filtered air for 1 min before plasma was applied at a pressure of 0.2 mbar for 10 s. To find the optimal  
129 plasma time, five different plasma timings (10 s, 20 s, 30 s, 60 s, and 120 s) were tested.

### 130 *2.2.3. PAMAM decoration of PS ESFs*

131 The plasma-generated carboxylic acid groups were activated by carbodiimide chemistry to decorate the  
132 surface of the fibers with PAMAM. Gold electrodes containing PS-plasma (10 s) treated ESFs were dipped  
133 in a 2 mL solution of EDC (0.4 M)/NHS (0.1 M) mixture in deionized water for 1 h. The electrodes were  
134 immediately immersed in an aqueous PAMAM solution for 4 h, rinsed with deionized water, and then dried  
135 at RT. To determine the optimal dendrimer concentration, three PAMAM solution concentrations of 0.5, 1,  
136 and 2 wt.% were investigated.

### 137 *2.2.4. Covalent immobilization of antibodies and blocking steps*

138 The PAMAM amine groups on the PS ESFs surface were activated to form a covalent bond with the Fc  
139 region of anti-IL-10 using glutaraldehyde as a coupling agent. For this purpose, the electrodes were put in  
140 a desiccator containing glutaraldehyde saturated vapor for overnight. Then, 20  $\mu$ L of anti-IL-10 (10  $\mu$ g/mL)  
141 was kept in contact with the ESF-modified electrodes for 1 h at 4 °C. After that, the immunosensor was  
142 carefully rinsed with PBS (10 mM, pH 7.4) and the blocking treatment was done by incubating it in 40  $\mu$ L  
143 of BSA 2% in PBS solution (10 mM, pH 7.4) for 1 h at 4 °C to reduce non-specific binding and deactivate  
144 the unbounded sites on the ESFs surface.

### 145 *2.3. Detection of AgIL-10 in PBS buffer and in artificial saliva (AS)*

146 The ESFs based immunosensor was immobilized in the electrochemical cell. The immunosensor was  
147 incubated in 40  $\mu$ L of different concentrations of AgIL-10 standard solution in PBS or AS for 30 min at

148 RT, followed by PBS washing to eliminate unbound AgIL-10 cytokine. The electrochemical cell was then  
149 filled with PBS (10 mM, pH 7.4) containing 5 mM  $K_3[Fe(CN)_6]/K_4[Fe(CN)_6]$  at each detection to record  
150 an EIS response. The electrolyte solution in the cell was withdrawn and the cell was washed with PBS  
151 solution after each EIS measurement.

#### 152 *2.4. Characterizations*

153 Instrumentation and procedures used for the physicochemical characterization are presented in the  
154 supplementary information.

#### 155 *2.5. Electrochemical measurements*

156 Instrumentation and procedures used for the electrochemical measurements are presented in the  
157 supplementary information.

### 158 **3. Results and discussion**

#### 159 *3.1. Choosing the optimal plasma time*

##### 160 *3.1.1. Morphological analysis*

161 Plasma-induced chemical changes are typically accompanied by morphological changes. It should be  
162 highlighted that extremely harsh surface treatment results in uneven surface etching, which has a significant  
163 influence on the immobilization and performance of bio-interface. The surface morphology influences the  
164 activity of immobilized biomolecules as well as the biophysical and chemical aspects of the biointerface,  
165 therefore picking the optimal time for plasma is crucial to minimize undesirable ion-assisted chemical  
166 etching and damage of PS fibers. [30] Five different times (10 s, 20 s, 30 s, 60 s, and 120 s) were tested to  
167 find the best plasma time for causing the least amount of damage to the PS ESFs surface and generating the  
168 most functional groups. The SEM images of ESFs are shown in Fig. S1. PS ESFs produced from  
169 electrospinning solution with a concentration of 20 wt.% had a bead-on-strings morphology, therefore a PS

170 solution with concentration of 25 wt.% was chosen to enhance polymer chain entanglement and produce  
171 fibers with a uniform morphology and reproducible characteristics (Fig. S1A).

172 According to the SEM images (Fig.S1 B-D), there are no signs of damage to the PS ESFs for 10 s, 20 s,  
173 and 30 s of plasma, but after that, the ESFs diameter begins to decrease (Fig. S1E and F). The mean diameter  
174 of pure PS ESFs was  $1805 \pm 336$  nm, while the diameter after 60 s of plasma decreased to  $1271 \pm 253$  nm.  
175 The ESFs structure was destroyed and the fibers were charred after 120 s of plasma. Consequently, using  
176 plasma to reduce fiber diameter for some specific purposes may be deemed a technique. Because PS ESFs  
177 were utilized as an interface in this study, their strength was especially crucial during the washing and  
178 immobilization processes. As a result, preserving their strength was prioritized, and SEM evaluation led to  
179 the selection of 10 s for plasma.

### 180 *3.1.2. wettability analysis*

181 Contact angle measurements were conducted to assess the involvement of plasma treatment in the creation  
182 of functional groups on the surface of PS ESFs and their hydrophilic characteristics. According to the results  
183 (Fig. S2), the contact angle of the PS ESFs after 10 s of plasma was  $0^\circ$ , while the contact angle of pure PS  
184 ESFs was  $145^\circ \pm 2.5^\circ$ . The formation of COOH, OH, C=O, and C–O, leads to the contact angle decreasing.  
185 [31] The production of singly and doubly bonded C–O functionality is based on the removal of hydrogen  
186 from tertiary C–H bonds or benzene rings, followed by oxygen substitution in free radical sites. [32]

187 A duration of 10 s was chosen as the optimal plasma time since it reduced the contact angle to  $0^\circ$  and  
188 caused the least amount of damage to the ESFs. It should be mentioned that fiber hydrophilicity is a key  
189 feature for the homogenous immobilization of antibodies on the fiber surface, as well as improved electron  
190 transfer between the electrolyte and the electrode.

## 191 *3.2. Evaluation of fiber-based immunosensor*

### 192 *3.2.1. FE-SEM characterization*

193 FE-SEM microscopic analysis of the fibers' surface before and after the plasma indicated that a plasma time  
194 of 10 s was appropriate since there were no signs of fracture or cracking on the surface of the fibers (Fig.  
195 1A-B). The significant difference between before and after the plasma is the rise in nanoporosity size on  
196 the surface of the fibers, which increases surface area and enhances potential interaction with the  
197 environment [33]. The fibers' morphology changed to peach skin after being decorated with PAMAM (Fig.  
198 1C). The average diameter of PS-plasma 10 s-PAMAM 2 wt.% ESFs was  $1565 \pm 290$  nm (Fig. 1D).

199 Fig. 1.

### 200 3.2.2. *fluorescence microscopy*

201 Fluorescence microscopy of PS ESFs revealed that plasma-modified PS fibers had autofluorescence ( $4.26$   
202  $\pm 1$ ) at 488 nm wavelength excitation as compared to pure PS (Fig. 2A-B). A high level of autofluorescence  
203 has been proven in thermoplastic polymers, including PS, particularly between the wavelengths of 300 -  
204 400 nm. A recent study has shown that thermal and solvent treatment increases the levels of  
205 autofluorescence of PS plate and changes its wavelength to longer wavelengths. [34] Here, the PS ESFs  
206 have no autofluorescence at 488 nm wavelength excitation, whereas autofluorescence and spots of different  
207 sizes are observed on the PS-plasma 10 s ESFs. The autofluorescence of PS fibers has been attributed to  
208 excimers resulting from polymer chain reorganization, which have longer wavelengths than the monomer  
209 emission peak. It should be noted that due to the high interest in the use of ESFs in various fields,  
210 particularly optical immunosensors, and the proximity of the fluorophores wavelength used for antibody  
211 conjugation to the plasma treated PS wavelength, serious consideration should be given to their  
212 autofluorescence after plasma to avoid false positive results. [34] Fig. 2C-E shows images of fibers after  
213 being decorated with various concentrations of PAMAM. Because PAMAM has fluorescence properties at  
214 488 nm excitation [19], the fluorescence increase in PS-plasma 10 s-PAMAM ESFs could be noticed when  
215 PAMAM concentration increases. The quantity of grafted PAMAM at the fiber surface is larger in the PS-  
216 plasma 10s-PAMAM 2 wt.% sample than in the other samples. The average fluorescence intensity for each  
217 of the mentioned ESFs was obtained by preparing 5 distinct samples and assessing 5 different points of

218 each sample. Fig. 2F shows the fluorescence intensities of different ESFs samples, according to which the  
219 fluorescence intensities for the 0.5, 1, and 2 wt.% dendrimer samples were  $30.5 \pm 4.4$ ,  $47.2 \pm 6.7$ , and  $60.8$   
220  $\pm 5.5$ , respectively. Because of its higher fluorescence properties, PS-plasma 10 s-PAMAM 2 wt.% was  
221 chosen as the best sample, and all immunosensors were prepared with this concentration.

222 Fig. 2.

### 223 3.2.3. FTIR analysis

224 ATR-FTIR analysis were done in order to more accurately evaluate the chemical composition of PS ESFs  
225 during the surface modification and immunosensor fabrication processes. The bands at  $3080\text{-}3024\text{ cm}^{-1}$ ,  
226  $2920\text{ cm}^{-1}$ , and  $2846\text{ cm}^{-1}$  in the PS spectra are attributable to aromatic C–H stretching vibration absorption  
227 and the presence of CH<sub>2</sub>, respectively. The peaks at  $1939\text{ cm}^{-1}$ ,  $1869\text{ cm}^{-1}$ ,  $1801\text{ cm}^{-1}$ , and  $1741\text{ cm}^{-1}$  are  
228 associated with overtone aromatic. The C=C stretching vibration absorption is seen at  $1600\text{ cm}^{-1}$ , while  
229 CH<sub>2</sub> bending vibrations are seen at  $1492\text{ cm}^{-1}$  and  $1451\text{ cm}^{-1}$  (Fig. 3Aa). [19] A comparison of spectra of  
230 PS and PS-plasma 10 s shows two new peaks at  $3454\text{ cm}^{-1}$  and  $1726\text{ cm}^{-1}$ , which correspond to OH and  
231 C=O from carboxylic acids, respectively (Fig. 3Ab). Fig. S3. depicts a schematic representation of the likely  
232 PS structure following plasma treatment. [31] According to previous study, the major mechanism for  
233 plasma treatment is an oxidative assault on the benzene ring followed by ring-opening to create  
234 aldehyde/carboxylate species. Oxidation of PS to a higher oxidation state and carbonyl/carboxyl species  
235 formation has been confirmed by IR-visible sum frequency generation (SFG) spectra. [35] The spectrum  
236 from PS-plasma 10 s-PAMAM 2 wt.% has amide bands of PAMAM  $\nu\text{NH}$  at  $3293\text{ cm}^{-1}$ ,  $\nu\text{CO}$  (amide I  
237 band) at  $1652\text{ cm}^{-1}$ ,  $\delta\text{NH}$  and  $\nu\text{CN}$  (amide II band) at  $1553\text{ cm}^{-1}$ . [29] It should be noted that the peak of  
238 carboxylic acid is decreased due to covalent bonding with PAMAM. Also, PS peaks are still present in the  
239 spectrum (Fig. 3Ac).

240 Previous studies have noted the N–H stretching vibration peak in the PAMAM dendrimer at  $3293\text{ cm}^{-1}$ ,  
241 which increased with increasing dendrimer concentration. [19,36] In the spectra of PS-plasma 10 s-

242 PAMAM 2 wt.%, a broad peak in the range of  $3100\text{ cm}^{-1}$  to  $3600\text{ cm}^{-1}$  is observed, which consists of two  
243 OH peaks in the region of  $3454\text{ cm}^{-1}$  formed by plasma modification and the amide bands  $\nu\text{NH}$  of PAMAM  
244 at  $3293\text{ cm}^{-1}$ , which are overlapped. When the two spectra in Fig. 3B are compared, the tip of the peak in  
245 the PS-plasma 10 s-PAMAM 2 wt.% spectra is placed near the N–H stretching vibration peak, confirming  
246 the presence of this peak of PAMAM in the spectrum.

247 The spectrum of PS-plasma 10 s-PAMAM 2 wt.%-glutaraldehyde before and after anti-IL-10 ( $10\text{ }\mu\text{g/mL}$ )  
248 immobilization is shown in Fig. 3Ca and b, respectively. Fig. 3Ca shows the characteristic peak at  $1715$   
249  $\text{cm}^{-1}$  for glutaraldehyde and also the peaks at  $1662\text{ cm}^{-1}$  and  $1552\text{ cm}^{-1}$  of the amide bands of PAMAM in  
250 the spectrum. After anti-IL-10 antibody immobilization, the glutaraldehyde peak at  $1715\text{ cm}^{-1}$  decreased  
251 significantly, indicating a covalent bond between the antibody and glutaraldehyde (Fig.3 Cb). [37,38]  
252 However, it should be noted that due to the peak overlap of PAMAM and anti-IL-10 amine groups, it is not  
253 possible to distinguish between them.

#### 254 3.2.4. UV–vis analysis

255 Fig. 3D shows the UV–visible absorption spectrum of the supernatant after washing PS-plasma 10 s-  
256 PAMAM-glutaraldehyde with washing buffer, PBS solution ( $10\text{ mM}$ , pH 7.4) for 5 min. An absorption  
257 peak is observed at  $235\text{ nm}$ , which is connected to the carbon – carbon double bond  $\pi - \pi^*$  transition of  
258 aldehyde groups. [39,40] According to the findings, the amount of unreacted glutaraldehyde in the  
259 supernatant is inversely linked to the concentration of PAMAM, so the PS-plasma 10 s-PAMAM 2 wt.%-  
260 glutaraldehyde supernatant has the lowest amount of glutaraldehyde adsorption. This shows that increasing  
261 the PAMAM concentration while also increasing the number of amine groups on the fiber surface induces  
262 more glutaraldehyde molecules to establish stronger covalent bonds with them.

263 Fig. 3.

#### 264 3.2.5. Electrochemical characterization

265 The ESFs modified-gold electrode in stepwise fabrication process of ESFs based immunosensor was  
266 evaluated by CV measurement in PBS (10 mM, pH 7.4) containing 5 mM  $[\text{Fe}(\text{CN})_6]^{3-/4-}$  because of any  
267 alterations in the bio-interface physically hinder the electrochemical behavior of the redox probe. As shown  
268 in Fig. 4A, the bare gold electrode presents well-defined anodic/cathodic peaks of  $[\text{Fe}(\text{CN})_6]^{3-/4-}$  and a  
269 reversible voltammogram with peak-to peak separation ( $\Delta E_p$ ) of  $\sim 182.5$  mV, with a peak maximum  
270 intensity ( $I_{pa} = 115.6 \mu\text{A}$ ). After electrospinning of the PS fibers on the electrode, the oxidation and redox  
271 peaks of the redox probe almost disappeared ( $I_{pa} = 14.6 \mu\text{A}$ ). Electron transfer from the electrolyte to the  
272 gold electrode surface happens as a result of tunneling through the porosity of the fibrous mats. The lack of  
273 conductivity and high hydrophobicity of the PS ESFs block the diffusion of redox probe to the electrode  
274 surface. Plasma modification for 10 s significantly increased the amperometric response of the electrode  
275 containing PS ESFs ( $I_{pa} = 113.5 \mu\text{A}$ ). The formation of oxygen-containing groups after plasma is the main  
276 factor contributing to the increasing mobility of the redox probe towards the electrode. [41] Modification  
277 of the fiber surface with PAMAM increased oxidation/reduction current ( $I_{pa} = 135.1 \mu\text{A}$ ) and decreased  
278  $\Delta E_p$  from  $\sim 210.5$  to  $\sim 186.5$  mV, which indicates the successful attachment of PAMAM at the PS fiber  
279 surface [29]. The pKa of the peripheral functional groups ( $-\text{NH}_3^+$ , pKa  $\sim 9.52$ ) gave the PAMAM a  
280 protonated interface in aqueous media at neutral pH. [42] Positively charged PAMAM accumulates the  
281 ferro/ferricyanide redox probe on its surface because of its electrostatic interaction. The electron-rich  
282 PAMAM surface amine groups and the electron-deficient interior create an electric field that accelerates  
283 electron transfer on the electrode's surface. [43] Fig. 4B depicts the role of PAMAM in increasing current  
284 response; when dendrimer concentration rose from 0.5 to 2 wt.% due to increased dendrimer presence at  
285 the fiber surface, the current increased from ( $I_{pa} = 121.7 \mu\text{A}$ ) to ( $I_{pa} = 135.1 \mu\text{A}$ ). The results were  
286 compatible with the fluorescence images in section 3.2.2. Due to improved electron transfer and a larger  
287 presence of amine groups on the surface, the concentration of 2 wt.% was determined as the best  
288 concentration for immunosensor preparation.

289 The CV responses of the PS-plasma 10 s-PAMAM 2 wt.-%-glutaraldehyde ESFs electrode at different scan  
 290 rates (10 to 100 mVs<sup>-1</sup>) are shown in Fig. S4A. Increasing the scan rate, which in turn reduces the  
 291 penetration layer, increases the current peak and ΔE<sub>p</sub>. Fig. S4B shows the square root of the scan rate versus  
 292 anodic and cathodic peak currents [ $I_{pa}(\mu A) = 14.8739 v^{1/2}[(mV/s)^{1/2}] + 9.2634. R^2 = 0.99$ ] and  
 293 [ $I_{pc}(\mu A) = -14.7623 v^{1/2}[(mV/s)^{1/2}] - 12.4408. R^2 = 0.99$ ], respectively. Fig. S4C shows the square  
 294 root of the scan rate versus anodic and cathodic peak potentials, [ $E_{pa}(V) = 0.0083 v^{1/2}[(mV/s)^{1/2}] +$   
 295  $0.2549. R^2 = 0.99$ ] and, [ $E_{pc}(V) = -0.0087 v^{1/2}[(mV/s)^{1/2}] + 0.1888. R^2 = 0.99$ ], respectively. Peak  
 296 currents and peak potentials of developed ESFs-based electrodes have a linear relationship with the square  
 297 root of the scan rate (square of regression coefficient of 0.99), demonstrating that the electron transfer  
 298 process in developed immunosensor is mostly based on a diffusion-controlled process. [44]

299 The electro-active surface area provided by the ESFs developed immunosensor was determined to be 0.149  
 300 cm<sup>2</sup> by the Randles–Sevcik equation  $I_p = 268600AD^{1/2}n^{3/2}Cv^{1/2}$  in which I<sub>p</sub> is the redox peak current  
 301 (A), A is electroactive surface area (cm<sup>2</sup>), D is the diffusion coefficient (D = 7.60 × 10<sup>-6</sup>, at 25 °C), n is  
 302 the number of electrons transferred in the redox reaction (n = 1), C is the concentration of the reactant (5  
 303 mM Fe(CN)<sub>6</sub><sup>3-/4-</sup>) (mol/cm<sup>3</sup>), and v is the scan rate (V/s). [45,46] For bare gold electrode, the electro-active  
 304 surface area of 0.127 cm<sup>2</sup> was measured, indicating the role of fibers in 17.3% increasing the available  
 305 surface-active area.

306 To evaluate ESFs based electrode's capability as an effective bio-interface, 40 μL of different concentrations  
 307 of anti-IL-10 were immobilized on the surface of the PS-plasma 10 s-PAMAM 2 wt.-%-glutaraldehyde ESFs  
 308 electrode at 4 °C for 1 h and the electrode characterized with CV measurement in PBS (10 mM, pH 7.4)  
 309 containing 5 mM [Fe(CN)<sub>6</sub>]<sup>3-/4-</sup> with a scan rate of 60 mV s<sup>-1</sup> (Fig. 4C). A drop in redox current was seen  
 310 following the immobilization of the antibody on the fiber surface due to the insulating characteristics of  
 311 antibodies and this was a valid indicator of successful grafting on the fiber surface. Increasing the antibody

312 concentration further reduced the anodic peak intensity, confirming the higher immobilized density of the  
313 antibody at the extraordinarily high available surface area provided by the fibers.

314 The activity of the anti-IL-10 on the surface of the fibers and the performance of the immunosensor before  
315 and after antigen incubation were also examined with CV in PBS (10 mM, pH 7.4) containing 5 mM  
316  $[\text{Fe}(\text{CN})_6]^{3-/4-}$  at the final stage of immunosensor preparation (Fig. 4D). The current of  $[\text{Fe}(\text{CN})_6]^{3-/4-}$  on  
317 PS-plasma 10 s-PAMAM 2 wt.% ESFs electrode was ( $I_{\text{pa}} = 130.4 \mu\text{A}$ ). After incubating 10 pg/mL of  
318 AgIL-10 on the electrode surface, the redox current ( $I_{\text{pa}} = 112.8 \mu\text{A}$ ) were lower than the PS-plasma 10  
319 s-PAMAM 2 wt.%-anti-IL-10-BSA current ( $I_{\text{pa}} = 124.0 \mu\text{A}$ ). This decrease is due to immune complexes  
320 formed by Anti-IL-10 and Ag-IL-10, which could obstruct electron transfer to the electrode surface as an  
321 insulating layer and confirms the developed ESFs immunosensor's high affinity for Ag-IL-10 cytokine.

322 The results of the developed immunosensor's stability after 20 consecutive cycles at a scan rate of  $60 \text{ mVs}^{-1}$   
323 are shown in Fig. S4D. The covalent bond between anti-IL-10 and glutaraldehyde, as well as the strong  
324 fiber adhesion to the electrode surface, resulted in constant redox peaks and peak potential separation, with  
325 relative standard deviations (RSDs) of 0.68 % and 0.87 % for  $I_{\text{pa}}$  and  $I_{\text{pc}}$ , respectively. [47]

### 326 3.3. Electrochemical detection of AgIL-10 in PBS

327 EIS was employed as a sensitive approach to assess antibody-antigen interactions at the immunosensor  
328 interface and to quantitatively determine AgIL-10 in PBS and AS. The presented EIS results in the Nyquist  
329 diagram for AgIL-10 detection from 1 pg/mL to 50 pg/mL in PBS (10 mM, pH 7.4) are shown in Fig. 4E,  
330 where the semicircle at higher frequencies refers to the electron transfer process and the linear section at  
331 low frequencies belongs to the diffusion process. The gray semicircle corresponds to the immobilization of  
332 10  $\mu\text{g/mL}$  of anti-IL-10 on the surface of the PS-plasma 10 s-PAMAM 2 wt.%-glutaraldehyde ESFs  
333 electrode for 1 h at 4 °C and shows low  $R_{\text{ct}}$ , which is consistent with the CV results and demonstrates the  
334 role of PAMAM in fast electron transfer and easily accessible redox probe to the electrode surface. As  
335 expected, after immobilization of each concentration of the AgIL-10 for 30 min at RT ( $20 \pm 1 \text{ }^\circ\text{C}$ ), the

336 diameter of semicircles increased owing to immunorecognition of AgIL-10 by surface-fixed antibodies that  
337 can hinder redox probe charge transfer as an electrical contact barrier. Furthermore, the results show that  
338 the proposed immunosensor has a high affinity for AgIL-10 with rising  $R_{ct}$ , due to the increased antigen  
339 steric hindrance on the electroactive interface for redox probe and restriction of the Faradaic reaction. [48]  
340 The electrochemical parameters were derived after each detection by fitting the Nyquist plots with the  
341 Randle's equivalent circuit, where  $R_s$  corresponds to the ohmic electrolyte resistance,  $Q_{CPE}$  to constant  
342 phase element,  $R_{ct}$  to charge transfer resistance, and  $\mathcal{W}$  to Warburg impedance (inset of Fig. 4E). The  
343 calibration diagram of immunosensor obtained from the impedance fitting data based on  $\Delta R/R$   
344  $, (R_{antigen} - R_{antibody})/R_{antibody}$ , versus different concentrations of AgIL-10 (1, 5, 10, 20, 35, and 50  
345 pg/mL) is shown in Fig. 4F. The immunosensor showed two linear correlation in the ranges from 1 pg/mL  
346 to 10 pg/mL with a linear regression equation of  $\Delta R/R = (0.03188 \pm 0.0018)[IL - 10] +$   
347  $0.21685 (\pm 0.01)$  and a correlation coefficient of  $R^2 = 0.99$ . The second range of 10 pg/mL to 50 pg/mL  
348 was similarly adjusted to a linear regression equation of  $\Delta R/R = (0.00838 \pm 0.0008)[IL - 10] +$   
349  $0.45164 (\pm 0.01)$ , with  $R^2 = 0.98$ . The smaller change in redox current at higher Ag-IL-10 concentrations,  
350 which led the calibration curve to be separated into two segments, is due to anti-IL-10 antibody saturation  
351 and a reduction of free antibodies available on the surface of the electrospun fibers to form an  
352 immunocomplex. The immunosensor has a limit of detection (LOD) of 1 pg/mL based on  $3 S/m$ , where  $S$   
353 represents the residual standard deviation and  $m$  denotes the slope of the regression line.

354 The inter- and intra-assay precisions of the results obtained using the designed immunosensor were studied.  
355 The inter-assay reproducibility of ESFs immunosensor was performed using five independent electrode  
356 prepared in the same manner for assessing samples containing 10 pg/mL of AgIL-10. While for the intra-  
357 assay, the same designed immunosensor was used five times to detect 10 pg/ml of AgIL-10. The RSD of  
358 inter- and intra-assay was around 3.18% and 0.79%, respectively. This result indicated that the developed  
359 ESFs immunosensor's precision, reproducibility, and repeatability were desirable.

360 Table 1 compares the analytical performance of the ESFs-based immunosensor to that of other  
361 immunosensors for the detection of IL-10 that have been reported to date. To our knowledge, this is the  
362 first study to use ESFs as an interface to detect IL-10. The increased surface area provided by the fibers  
363 permitted a significantly higher number of antibodies on the surface (100  $\mu\text{g}/\text{mL}$ ) and provided a  
364 comparable detection range and extremely low detection limit to previous studies.

365 Fig. 4.

366 Table 1.

### 367 *3.4. Interference study*

368 To evaluate the specificity of the immunosensor, an aliquot of 20  $\mu\text{L}$  of anti-IL-10 (10  $\mu\text{g}/\text{mL}$ ) was fixed  
369 on the ESF modified-gold electrode at 4  $^{\circ}\text{C}$  for 1 h and 40  $\mu\text{L}$  of TNF-alpha antigen with different  
370 concentrations (1, 5, 10, and 20  $\text{pg}/\text{mL}$ ) was incubated with the ESF modified-gold electrode at RT for 30  
371 min. The results of the interference studies in Fig. 5A show that the developed immunosensor is selective  
372 for AgIL-10.

### 373 *3.5. Electrochemical detection of AgIL-10 in AS*

374 The function of the immunosensor for AgIL-10 detection in AS as a complex medium and natural saliva  
375 simulator was assessed by EIS. The EIS concepts and immunosensor fabrication procedures were the same  
376 as mentioned before. Initially, the likelihood of any unspecific absorption by AS was examined by  
377 incubating 40  $\mu\text{L}$  of it on the surface of the ESFs electrode (without AgIL-10). Fig. 5B shows the 3 times  
378 incubation of AS on the ESFs immunosensor. After the first incubation of AS, an increase in  $R_{\text{ct}}$  was  
379 observed. This impact was detected in all AS measures in this investigation and is thus considered a  
380 constant. The matrix effect, also known as unspecific adsorption, has been discovered in prior  
381 investigations. [49] Re-incubation of AS (second and third semicircles) did not result in increased  
382 impedance or undesired absorption. It should be emphasized that the immunosensor surface was thoroughly  
383 washed with PBS between each incubation step. Fig. 5C shows the Nyquist plot for the detection of AgIL-

384 10 in AS. After 3 times incubation of AS and maintaining a consistent  $R_{ct}$ , the AS containing various  
385 concentrations of AgIL-10 (10, 25, 50, and 100 pg/mL) was applied to the fiber surface for 30 min at RT  
386 each time. The detection of AgIL-10 in AS as a complex medium is highlighted by increasing the Nyquist  
387 plot semicircle each time. Furthermore, the EIS signal displayed a linear relationship with IL-10  
388 concentrations ranging from 10-100 pg/mL and a LOD of 4,63 pg/mL, with a regression equation of  
389  $\Delta R/R = (0.00483 \pm 0.0002)[IL - 10] + 0.00382 (\pm 0.008)$  and a correlation coefficient of  $R^2 = 0,96$   
390 (Fig. 5D).

391 Fig. 5.

#### 392 4. Conclusion

393 In this study, PAMAM polymer was used to decorate the air plasma-modified PS electrospun fibers' surface,  
394 resulting in the development of a 3-D open-porous interface and an impedimetric immunosensor with very  
395 high sensitivity to the IL-10 cytokine. The formation of carboxylic acid functional groups on fiber surfaces,  
396 a rise in hydrophilicity, and the creation of autofluorescence characteristics in PS fibers were all induced  
397 by 10 s of air plasma. Increased PAMAM concentration on the fiber surface causes more glutaraldehyde  
398 molecules to form covalent bonds with them. Anti-IL-10 capture antibody was successfully immobilized  
399 on the PS fiber surface by glutaraldehyde coupling chemistry on the amine functional groups of PAMAM.  
400 The immunosensor showed ameliorated stability due to covalent bonding between PAMAM amine groups  
401 and anti-IL-10 using a glutaraldehyde coupling agent. Modification of the fiber surface with PAMAM  
402 increased oxidation/reduction current and promoted antibody immobilization by increasing surface area.  
403 The PS-plasma-PAMAM 2 wt.% ESFs-based immunosensor is a new 3-D framework with great sensitivity  
404 and selectivity within a wide linear range of AgIL-10 detection in both PBS and AS. The proposed ESFs  
405 based interface is a promising material that can be employed in the clinical detection of cytokines or as a  
406 substrate for immunosensors development.

#### 407 Acknowledgements

408 P.R. thanks the Ministry of Science, Research and Technology of the Islamic Republic of Iran for providing  
409 the scholarship. The authors acknowledge the financial support of the EU H2020 WIDESPREAD Program  
410 entitled Bionanosens grant agreement # 951887. Campus France is acknowledged for the financial support  
411 through PHC Maghreb EMBISALIM.

## 412 References

413

- 414 [1] H. Han, Q. Ma, C. Li, R. Liu, L. Zhao, W. Wang, P. Zhang, X. Liu, G. Gao, F. Liu, Y. Jiang, X.  
415 Cheng, C. Zhu, Y. Xia, Profiling serum cytokines in COVID-19 patients reveals IL-6 and IL-10  
416 are disease severity predictors, *Emerg. Microbes Infect.* 9 (2020) 1123–1130.  
417 <https://doi.org/10.1080/22221751.2020.1770129>.
- 418 [2] W. Udomsinprasert, J. Jittikoon, S. Sangroongruangsri, Circulating levels of interleukin-6 and  
419 interleukin-10, but not tumor necrosis factor-alpha, as potential biomarkers of severity and  
420 mortality for COVID-19: systematic review with meta-analysis, *J. Clin. Immunol.* (2020) 1–12.
- 421 [3] H. Islam, T.C. Chamberlain, A.L. Mui, J.P. Little, Elevated interleukin-10 levels in COVID-19:  
422 potentiation of pro-inflammatory responses or impaired anti-inflammatory action?, *Front.*  
423 *Immunol.* (2021) 2485.
- 424 [4] F. Nessark, M. Eissa, A. Baraket, N. Zine, B. Nessark, A. Zouaoui, J. Bausells, A. Errachid,  
425 Capacitance Polypyrrole-based Impedimetric Immunosensor for Interleukin-10 Cytokine  
426 Detection, *Electroanalysis.* 32 (2020) 1795–1806. <https://doi.org/10.1002/elan.201900633>.
- 427 [5] M. Lee, N. Zine, A. Baraket, M. Zabala, F. Campabadal, R. Caruso, M.G. Trivella, N. Jaffrezic-  
428 Renault, A. Errachid, A novel biosensor based on hafnium oxide: Application for early stage  
429 detection of human interleukin-10, *Sensors Actuators, B Chem.* 175 (2012) 201–207.  
430 <https://doi.org/10.1016/j.snb.2012.04.090>.
- 431 [6] Q. Lu, Z. Zhu, C. Tan, H. Zhou, Y. Hu, G. Shen, P. Zhu, G. Yang, X. Xie, Changes of serum IL-  
432 10, IL-1 $\beta$ , IL-6, MCP-1, TNF- $\alpha$ , IP-10 and IL-4 in COVID-19 patients, *Int. J. Clin. Pract.* 75  
433 (2021) e14462.
- 434 [7] M. Zimecki, J.K. Actor, M.L. Kruzel, The potential for Lactoferrin to reduce SARS-CoV-2  
435 induced cytokine storm, *Int. Immunopharmacol.* 95 (2021).  
436 <https://doi.org/10.1016/j.intimp.2021.107571>.
- 437 [8] V. Azmy, K. Kaman, D. Tang, H. Zhao, C. Dela Cruz, J.E. Topal, M. Malinis, C.C. Price,  
438 Cytokine profiles before and after immune modulation in hospitalized patients with COVID-19, *J.*  
439 *Clin. Immunol.* 41 (2021) 738–747.
- 440 [9] J.G. de Oliveira Santos, D.P. Migueis, J.B. do Amaral, A.L.L. Bachi, A.C. Boggi, A. Thamboo,  
441 R.L. Voegels, R. Pezato, Impact of SARS-CoV-2 on saliva: TNF- $\alpha$ , IL-6, IL-10, lactoferrin,  
442 lysozyme, IgG, IgA, and IgM, *J. Oral Biosci.* 64 (2022) 108–113.
- 443 [10] M. Bahri, A. Baraket, N. Zine, M. Ben Ali, J. Bausells, A. Errachid, Capacitance electrochemical  
444 biosensor based on silicon nitride transducer for TNF- $\alpha$  cytokine detection in artificial human  
445 saliva: Heart failure (HF), *Talanta.* 209 (2020) 120501.  
446 <https://doi.org/10.1016/j.talanta.2019.120501>.

- 447 [11] A. Baraket, M. Lee, N. Zine, M. Sigaud, J. Bausells, A. Errachid, A fully integrated  
448 electrochemical biosensor platform fabrication process for cytokines detection, *Biosens.*  
449 *Bioelectron.* 93 (2017) 170–175. <https://doi.org/10.1016/j.bios.2016.09.023>.
- 450 [12] R. Pruna, F. Palacio, A. Baraket, N. Zine, A. Streklas, J. Bausells, A. Errachid, M. López, A low-  
451 cost and miniaturized potentiostat for sensing of biomolecular species such as TNF- $\alpha$  by  
452 electrochemical impedance spectroscopy, *Biosens. Bioelectron.* 100 (2018) 533–540.  
453 <https://doi.org/10.1016/j.bios.2017.09.049>.
- 454 [13] C. Karaman, B.B. Yola, O. Karaman, N. Atar, İ. Polat, M.L. Yola, Sensitive sandwich-type  
455 electrochemical SARS-CoV-2 nucleocapsid protein immunosensor, *Microchim. Acta.* 188 (2021)  
456 1–13.
- 457 [14] C. Karaman, Ö.S. Bölükbaşı, B.B. Yola, O. Karaman, N. Atar, M.L. Yola, Electrochemical  
458 neuron-specific enolase (NSE) immunosensor based on CoFe<sub>2</sub>O<sub>4</sub>@ Ag nanocomposite and  
459 AuNPs@ MoS<sub>2</sub>/rGO, *Anal. Chim. Acta.* 1200 (2022) 339609.
- 460 [15] H. Boyacıoğlu, B.B. Yola, C. Karaman, O. Karaman, N. Atar, M.L. Yola, A novel electrochemical  
461 kidney injury molecule-1 (KIM-1) immunosensor based covalent organic frameworks-gold  
462 nanoparticles composite and porous NiCo<sub>2</sub>S<sub>4</sub>@ CeO<sub>2</sub> microspheres: the monitoring of acute  
463 kidney injury, *Appl. Surf. Sci.* 578 (2022) 152093.
- 464 [16] O. Karaman, N. Özcan, C. Karaman, B.B. Yola, N. Atar, M.L. Yola, Electrochemical cardiac  
465 troponin I immunosensor based on nitrogen and boron-doped graphene quantum dots electrode  
466 platform and Ce-doped SnO<sub>2</sub>/SnS<sub>2</sub> signal amplification, *Mater. Today Chem.* 23 (2022) 100666.
- 467 [17] M.L. Yola, N. Atar, Carbohydrate antigen 19-9 electrochemical immunosensor based on 1D-  
468 MoS<sub>2</sub> nanorods/LiNb<sub>3</sub>O<sub>8</sub> and polyoxometalate-incorporated gold nanoparticles, *Microchem. J.*  
469 170 (2021) 106643.
- 470 [18] T. Yang, L. Zhan, C.Z. Huang, Recent insights into functionalized electrospun nanofibrous films  
471 for chemo-/bio-sensors, *TrAC - Trends Anal. Chem.* 124 (2020).  
472 <https://doi.org/10.1016/j.trac.2020.115813>.
- 473 [19] P. Razmshoar, S.H. Bahrami, M. Rabiee, M. Hangouet, M. Martin, G. Raffin, A. Errachid, N.  
474 Jaffrezic-Renault, Novel platform based on polystyrene electrospun nanofibrous mats doped with  
475 PAMAM dendritic polymer for enhanced immunosensing, *Appl. Surf. Sci.* (2021) 152221.
- 476 [20] D.M. Dos Santos, D.S. Correa, E.S. Medeiros, J.E. Oliveira, L.H.C. Mattoso, Advances in  
477 functional polymer nanofibers: From spinning fabrication techniques to recent biomedical  
478 applications, *ACS Appl. Mater. Interfaces.* 12 (2020) 45673–45701.
- 479 [21] M. Adabi, S.S. Esnaashari, M. Adabi, An electrochemical immunosensor based on electrospun  
480 carbon nanofiber mat decorated with gold nanoparticles and carbon nanotubes for the detection of  
481 breast cancer, *J. Porous Mater.* 28 (2021) 415–421. <https://doi.org/10.1007/s10934-020-01004-w>.
- 482 [22] J. Xue, T. Wu, Y. Dai, Y. Xia, Electrospinning and electrospun nanofibers: Methods, materials,  
483 and applications, *Chem. Rev.* 119 (2019) 5298–5415.
- 484 [23] K.S. Ogueri, C.T. Laurencin, Nanofiber technology for regenerative engineering, *ACS Nano.* 14  
485 (2020) 9347–9363.
- 486 [24] B. Rezaei, A.M. Shoushtari, M. Rabiee, L. Uzun, A.P.F. Turner, W. Cheung Mak, Multifactorial  
487 modeling and optimization of solution and electrospinning parameters to generate superfine  
488 polystyrene nanofibers, *Adv. Polym. Technol.* 37 (2018) 2743–2755.  
489 <https://doi.org/10.1002/adv.21947>.

- 490 [25] A. Morelli, M.J. Hawker, Utilizing Radio Frequency Plasma Treatment to Modify Polymeric  
491 Materials for Biomedical Applications, *ACS Biomater. Sci. Eng.* (2021).  
492 <https://doi.org/10.1021/acsbiomaterials.0c01673>.
- 493 [26] S. Sathish, N. Ishizu, A.Q. Shen, Air Plasma-Enhanced Covalent Functionalization of Poly(methyl  
494 methacrylate): High-Throughput Protein Immobilization for Miniaturized Bioassays, *ACS Appl.*  
495 *Mater. Interfaces.* 11 (2019) 46350–46360. <https://doi.org/10.1021/acsami.9b14631>.
- 496 [27] F. Li, J. Peng, Q. Zheng, X. Guo, H. Tang, S. Yao, Carbon nanotube-polyamidoamine dendrimer  
497 hybrid-modified electrodes for highly sensitive electrochemical detection of microRNA24, *Anal.*  
498 *Chem.* 87 (2015) 4806–4813. <https://doi.org/10.1021/acs.analchem.5b00093>.
- 499 [28] A. Miodek, N. Mejri, M. Gomgnimbou, C. Sola, H. Korri-Youssoufi, E-DNA Sensor of  
500 *Mycobacterium tuberculosis* Based on Electrochemical Assembly of Nanomaterials  
501 (MWCNTs/PPy/PAMAM), *Anal. Chem.* 87 (2015) 9257–9264.  
502 <https://doi.org/10.1021/acs.analchem.5b01761>.
- 503 [29] P. Razmshoar, S. Hajir Bahrami, M. Rabiee, M. Hangouet, M. Martin, A. Errachid, N. Jaffrezic-  
504 Renault, A novel electrochemical immunosensor for ultrasensitive detection of tumor necrosis  
505 factor  $\alpha$  based on polystyrene - PAMAM dendritic polymer blend nanofibers, *Microchem. J.* 175  
506 (2022) 107206. <https://doi.org/10.1016/j.microc.2022.107206>.
- 507 [30] S.H. North, E.H. Lock, C.J. Cooper, J.B. Franek, C.R. Taitt, S.G. Walton, Plasma-based surface  
508 modification of polystyrene microtiter plates for covalent immobilization of biomolecules, *ACS*  
509 *Appl. Mater. Interfaces.* 2 (2010) 2884–2891. <https://doi.org/10.1021/am100566e>.
- 510 [31] A. Suganya, G. Shanmugvelayutham, J. Hidalgo-Carrillo, Plasma Surface Modified Polystyrene  
511 and Grafted with Chitosan Coating for Improving the Shelf Lifetime of Postharvest Grapes,  
512 *Plasma Chem. Plasma Process.* 38 (2018) 1151–1168. <https://doi.org/10.1007/s11090-018-9908-0>.
- 513 [32] E.H. Lock, D.Y. Petrovykh, P. Mack, T. Carney, R.G. White, S.G. Walton, R.F. Fernsler, Surface  
514 composition, chemistry, and structure of polystyrene modified by electron-beam-generated  
515 plasma, *Langmuir.* 26 (2010) 8857–8868. <https://doi.org/10.1021/la9046337>.
- 516 [33] M. Dufay, M. Jimenez, S. Degoutin, Effect of Cold Plasma Treatment on Electrospun Nanofibers  
517 Properties: A Review, *ACS Appl. Bio Mater.* 3 (2020) 4696–4716.  
518 <https://doi.org/10.1021/acsabm.0c00154>.
- 519 [34] E.W.K. Young, E. Berthier, D.J. Beebe, Assessment of enhanced autofluorescence and impact on  
520 cell microscopy for microfabricated thermoplastic devices, *Anal. Chem.* 85 (2013) 44–49.
- 521 [35] D. Zhang, S.M. Dougal, M.S. Yeganeh, Effects of UV irradiation and plasma treatment on a  
522 polystyrene surface studied by IR-visible sum frequency generation spectroscopy, *Langmuir.* 16  
523 (2000) 4528–4532. <https://doi.org/10.1021/la991353i>.
- 524 [36] H. Lu, L. Feng, S. Li, J. Zhang, H. Lu, S. Feng, Unexpected strong blue photoluminescence  
525 produced from the aggregation of unconventional chromophores in novel siloxane–poly  
526 (amidoamine) dendrimers, *Macromolecules.* 48 (2015) 476–482.
- 527 [37] M. Mahmoudifard, M. Soleimani, M. Vossoughi, Ammonia plasma-treated electrospun  
528 polyacrylonitrile nanofibrous membrane: The robust substrate for protein immobilization through  
529 glutaraldehyde coupling chemistry for biosensor application, *Sci. Rep.* 7 (2017) 1–14.  
530 <https://doi.org/10.1038/s41598-017-10040-7>.
- 531 [38] C.H. Chuang, H.P. Wu, Y.W. Huang, C.H. Chen, Enhancing of intensity of fluorescence by DEP  
532 manipulations of polyaniline-coated Al<sub>2</sub>O<sub>3</sub> nanoparticles for immunosensing, *Biosens.*

- 533 Bioelectron. 48 (2013) 158–164. <https://doi.org/10.1016/j.bios.2013.03.064>.
- 534 [39] H.K. Purss, G.G. Qiao, D.H. Solomon, Effect of “glutaraldehyde” functionality on network  
535 formation in poly(vinyl alcohol) membranes, *J. Appl. Polym. Sci.* 96 (2005) 780–792.  
536 <https://doi.org/10.1002/app.21511>.
- 537 [40] S. Tang, W. Ma, G. Xie, Y. Su, Y. Jiang, Acetylcholinesterase-reduced graphene oxide hybrid  
538 films for organophosphorus neurotoxin sensing via quartz crystal microbalance, *Chem. Phys. Lett.*  
539 660 (2016) 199–204. <https://doi.org/10.1016/j.cplett.2016.08.025>.
- 540 [41] J.Y. Lee, E.J. Park, C.J. Lee, S.W. Kim, J.J. Pak, N.K. Min, Flexible electrochemical biosensors  
541 based on O<sub>2</sub> plasma functionalized MWCNT, *Thin Solid Films.* 517 (2009) 3883–3887.  
542 <https://doi.org/10.1016/j.tsf.2009.01.130>.
- 543 [42] E. Bustos, J.E. García, Y. Bandala, L.A. Godínez, E. Juaristi, Enantioselective recognition of  
544 alanine in solution with modified gold electrodes using chiral PAMAM dendrimers G4.0, *Talanta.*  
545 78 (2009) 1352–1358. <https://doi.org/10.1016/j.talanta.2009.02.010>.
- 546 [43] Y. Zhou, J. He, C. Zhang, J. Li, X. Fu, W. Mao, W. Li, C. Yu, Novel Ce (III)-metal organic  
547 framework with a luminescent property to fabricate an electrochemiluminescence immunosensor,  
548 *ACS Appl. Mater. Interfaces.* 12 (2019) 338–346.
- 549 [44] L. Li, Y. Wang, L. Pan, Y. Shi, W. Cheng, Y. Shi, G. Yu, A nanostructured conductive hydrogels-  
550 based biosensor platform for human metabolite detection, *Nano Lett.* 15 (2015) 1146–1151.  
551 <https://doi.org/10.1021/nl504217p>.
- 552 [45] Y. He, S. Xie, X. Yang, R. Yuan, Y. Chai, Electrochemical Peptide Biosensor Based on in Situ  
553 Silver Deposition for Detection of Prostate Specific Antigen, *ACS Appl. Mater. Interfaces.* 7  
554 (2015) 13360–13366. <https://doi.org/10.1021/acsami.5b01827>.
- 555 [46] P. Zhu, Y. Zhao, Cyclic voltammetry measurements of electroactive surface area of porous nickel:  
556 peak current and peak charge methods and diffusion layer effect, *Mater. Chem. Phys.* 233 (2019)  
557 60–67.
- 558 [47] B. Rezaei, A.M. Shoushtari, M. Rabiee, L. Uzun, W.C. Mak, A.P.F. Turner, An electrochemical  
559 immunosensor for cardiac Troponin I using electrospun carboxylated multi-walled carbon  
560 nanotube-whiskered nanofibres, *Talanta.* 182 (2018) 178–186.  
561 <https://doi.org/10.1016/j.talanta.2018.01.046>.
- 562 [48] S. Palanisamy, D. Senthil Raja, B. Subramani, T.H. Wu, Y.M. Wang, Label-Free Bimetallic in  
563 Situ-Grown 3D Nickel-Foam-Supported NH<sub>2</sub>-MIL-88B(Fe<sub>2</sub>Co)-MOF-based Impedimetric  
564 Immunosensor for the Detection of Cardiac Troponin i, *ACS Appl. Mater. Interfaces.* 12 (2020)  
565 32468–32476. <https://doi.org/10.1021/acsami.0c09086>.
- 566 [49] F.G. Bellagambi, A. Baraket, A. Longo, M. Vatteroni, N. Zine, J. Bausells, R. Fuoco, F. Di  
567 Francesco, P. Salvo, G.S. Karanasiou, D.I. Fotiadis, A. Menciassi, A. Errachid, Electrochemical  
568 biosensor platform for TNF- $\alpha$  cytokines detection in both artificial and human saliva: Heart  
569 failure, *Sensors Actuators, B Chem.* 251 (2017) 1026–1033.  
570 <https://doi.org/10.1016/j.snb.2017.05.169>.
- 571 [50] M.M. Eissa, M. Mahbubor Rahman, N. Zine, N. Jaffrezic, A. Errachid, H. Fessi, A. Elaissari,  
572 Reactive magnetic poly(divinylbenzene-co-glycidyl methacrylate) colloidal particles for specific  
573 antigen detection using microcontact printing technique, *Acta Biomater.* 9 (2013) 5573–5582.  
574 <https://doi.org/10.1016/j.actbio.2012.10.027>.
- 575 [51] A. Baraket, M. Lee, N. Zine, M. Sigaud, N. Yaakoubi, M.G. Trivella, M. Zabala, J. Bausells, N.

- 576 Jaffrezic-Renault, A. Errachid, Diazonium modified gold microelectrodes onto polyimide  
577 substrates for impedimetric cytokine detection with an integrated Ag/AgCl reference electrode,  
578 *Sensors Actuators, B Chem.* 189 (2013) 165–172. <https://doi.org/10.1016/j.snb.2013.02.088>.
- 579 [52] A. Garcia-Cruz, M. Lee, N. Zine, M. Sigaud, J. Bausells, A. Errachid, Poly(pyrrole) microwires  
580 fabrication process on flexible thermoplastics polymers: Application as a biosensing material,  
581 *Sensors Actuators, B Chem.* 221 (2015) 940–950. <https://doi.org/10.1016/j.snb.2015.06.084>.
- 582 [53] P. Chen, M.T. Chung, W. McHugh, R. Nidetz, Y. Li, J. Fu, T.T. Cornell, T.P. Shanley, K.  
583 Kurabayashi, Multiplex serum cytokine immunoassay using nanoplasmonic biosensor  
584 microarrays, *ACS Nano.* 9 (2015) 4173–4181.
- 585 [54] A. Baraket, M. Lee, N. Zine, N. Yaakoubi, J. Bausells, A. Errachid, A flexible electrochemical  
586 micro lab-on-chip: application to the detection of interleukin-10, *Microchim. Acta.* 183 (2016)  
587 2155–2162. <https://doi.org/10.1007/s00604-016-1847-y>.
- 588 [55] C. Li, Y. Liu, X. Zhou, Y. Wang, A paper-based SERS assay for sensitive duplex cytokine  
589 detection towards the atherosclerosis-associated disease diagnosis, *J. Mater. Chem. B.* 8 (2020)  
590 3582–3589.
- 591 [56] S.H. Baek, H.W. Song, S. Lee, J.-E. Kim, Y.H. Kim, J.-S. Wi, J.G. Ok, J.S. Park, S. Hong, M.K.  
592 Kwak, Gold nanoparticle-enhanced and roll-to-roll nanoimprinted LSPR platform for detecting  
593 interleukin-10, *Front. Chem.* 8 (2020) 285.
- 594 [57] K. Parate, S. V. Rangnekar, D. Jing, D.L. Mendivelso-Perez, S. Ding, E.B. Secor, E.A. Smith,  
595 J.M. Hostetter, M.C. Hersam, J.C. Claussen, Aerosol-Jet-Printed Graphene Immunosensor for  
596 Label-Free Cytokine Monitoring in Serum, *ACS Appl. Mater. Interfaces.* 12 (2020) 8592–8603.  
597 <https://doi.org/10.1021/acsami.9b22183>.
- 598 [58] A. Occhicone, P. Del Porto, N. Danz, P. Munzert, A. Sinibaldi, F. Michelotti, Enhanced  
599 Fluorescence Detection of Interleukin 10 by Means of 1D Photonic Crystals, *Crystals.* 11 (2021)  
600 1517.
- 601
- 602
- 603
- 604
- 605
- 606
- 607
- 608
- 609
- 610
- 611
- 612

613  
614  
615  
616  
617  
618  
619

## 620 **Figure Captions**

621 Schematic.1. The schematic depicts the step-by-step preparation procedure for the developed  
622 immunosensor.

623 Fig. 1. FE-SEM images of A) pure PS, B) PS after 10 s plasma treatment, C) PS-plasma 10 s-PAMAM 2  
624 wt.% ESFs, and D) the diameter distribution of PS-plasma 10 s-PAMAM 2 wt.% ESFs.

625 Fig. 2. Fluorescence images of A) pure PS, B) PS-plasma 10 s, C) PS-plasma 10 s-PAMAM 0.5 wt.%, D)  
626 PS-plasma 10 s-PAMAM 1 wt.%, E) PS-plasma 10 s-PAMAM 2 wt.%, and F) quantification of fluorescent  
627 intensity of different samples (a) pure PS, (b) PS-plasma 10 s, (c) PS-plasma 10 s-PAMAM 0.5 wt.%, (d)  
628 PS-plasma 10 s-PAMAM 1 wt.%, and (e) PS-plasma 10 s-PAMAM 2 wt.%.

629 Fig. 3. A) ATR-FTIR spectra of (a) pure PS, (b) PS-plasma 10 s, and (c) PS-plasma 10 s-PAMAM 2 wt.%  
630 ESFs, B) zoom at  $3000-4000\text{ cm}^{-1}$ , C) (a) PS-plasma 10 s-PAMAM 2 wt.%-glutaraldehyde and (b) PS-  
631 plasma 10 s-PAMAM-2 wt.%-glutaraldehyde-anti-IL-10, and D) UV-vis spectra of unreacted  
632 glutaraldehyde in (a) PS-plasma 10 s-PAMAM 0.5 wt.%-glutaraldehyde, (b) PS-plasma 10 s-PAMAM 1  
633 wt.%-glutaraldehyde, (c) PS-plasma 10 s-PAMAM 2 wt.%-glutaraldehyde, and (d) pure PS.

634 Fig. 4. A) CVs of different stages of immunosensor preparation, B) CV of PS-plasma 10 s-PAMAM with  
635 different concentrations electrode, C) effect of different immobilized anti-IL-10 concentrations (10, 20, 40,  
636 50, and 100  $\mu\text{g/mL}$ ) on reducing the redox current, D) evaluation of anti-IL-10 activity (10  $\mu\text{g/mL}$ ) on the  
637 fiber surface, E) Nyquist plots of PS-plasma 10 s-PAMAM 2 wt.%-glutaraldehyde-anti-IL-10 modified gold

638 electrode of AgIL-10 detection ranging from 1 to 50 pg/mL, and F) calibration curves of the ESFs based  
639 immunosensors for the detection of AgIL-10.

640 Fig. 5. A) Selectivity results of the developed immunosensors, B) Nyquist plots of three times incubation  
641 of AS (without AgIL-10) on PS-plasma 10 s-PAMAM 2 wt.% ESFs modified gold electrode, C) Nyquist  
642 plots of the immunosensor for AgIL-10 detection in AS, and D) detection calibration curves of the  
643 immunosensor toward AgIL-10 in AS.

644 Table 1. Comparison of analytical characteristics of other immunosensors reported so far for IL-10  
645 detection with the presented ESFs based immunosensor.

646

647

648

649

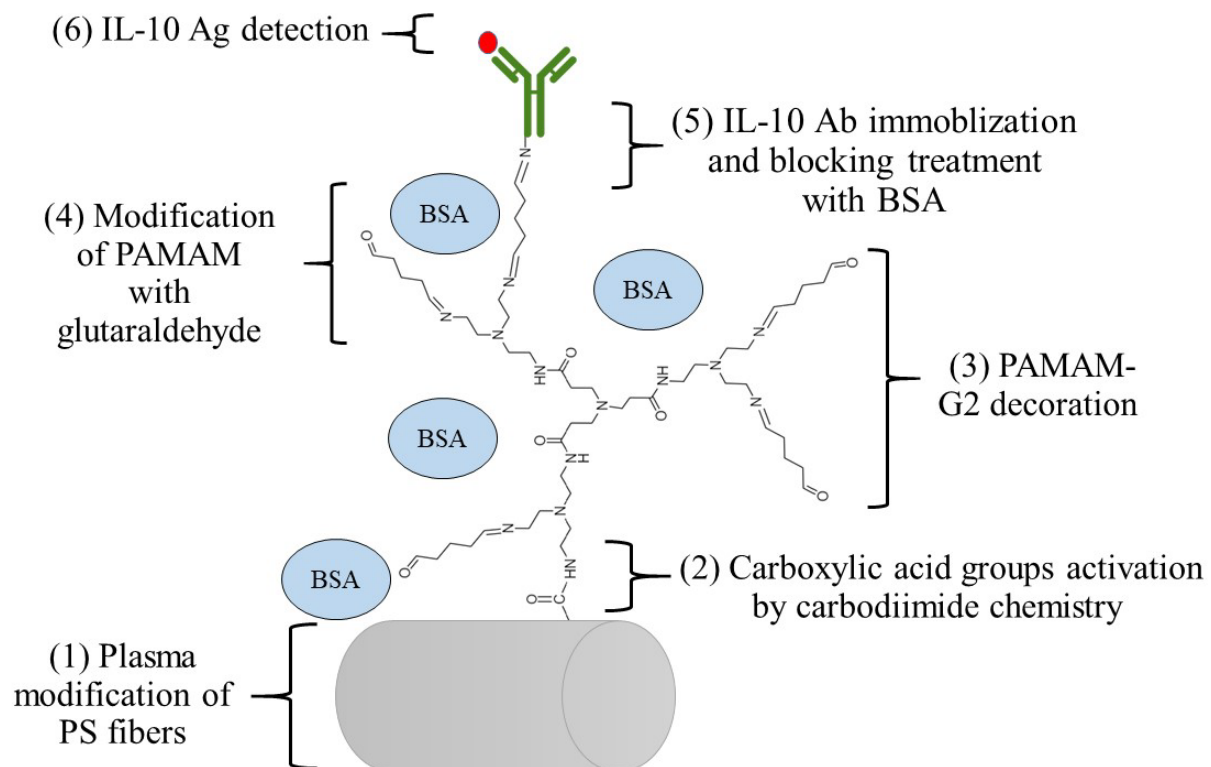
650

651

652

653

654



655

656 Schematic.1. The schematic depicts the step-by-step preparation procedure for the developed  
 657 immunosensor.

658

659

660

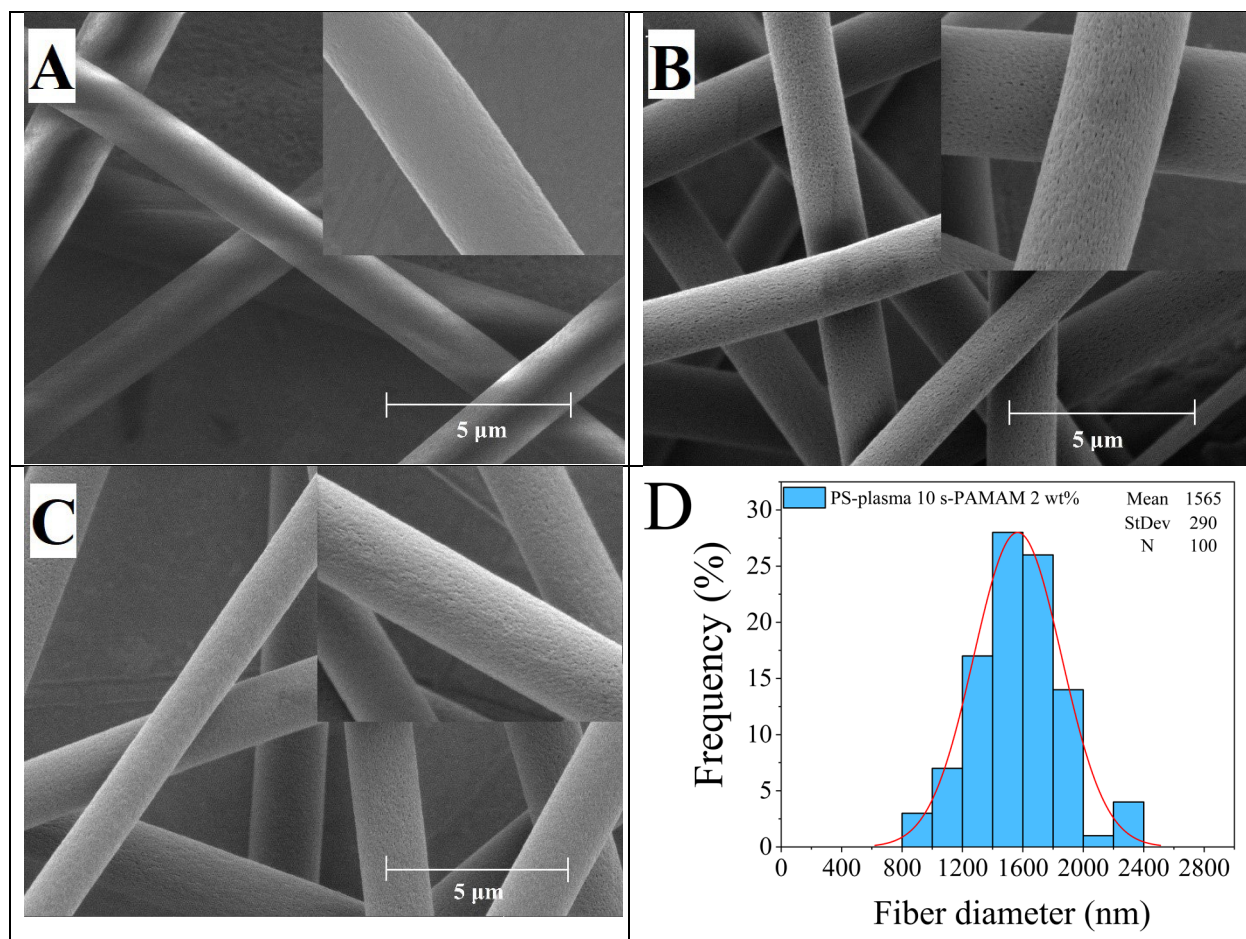
661

662

663

664

665



666

667 Fig. 1. FE-SEM images of A) pure PS, B) PS after 10 s plasma treatment, C) PS-plasma 10 s-PAMAM 2  
668 wt.% ESFs, and D) the diameter distribution of PS-plasma 10 s-PAMAM 2 wt.% ESFs.

669

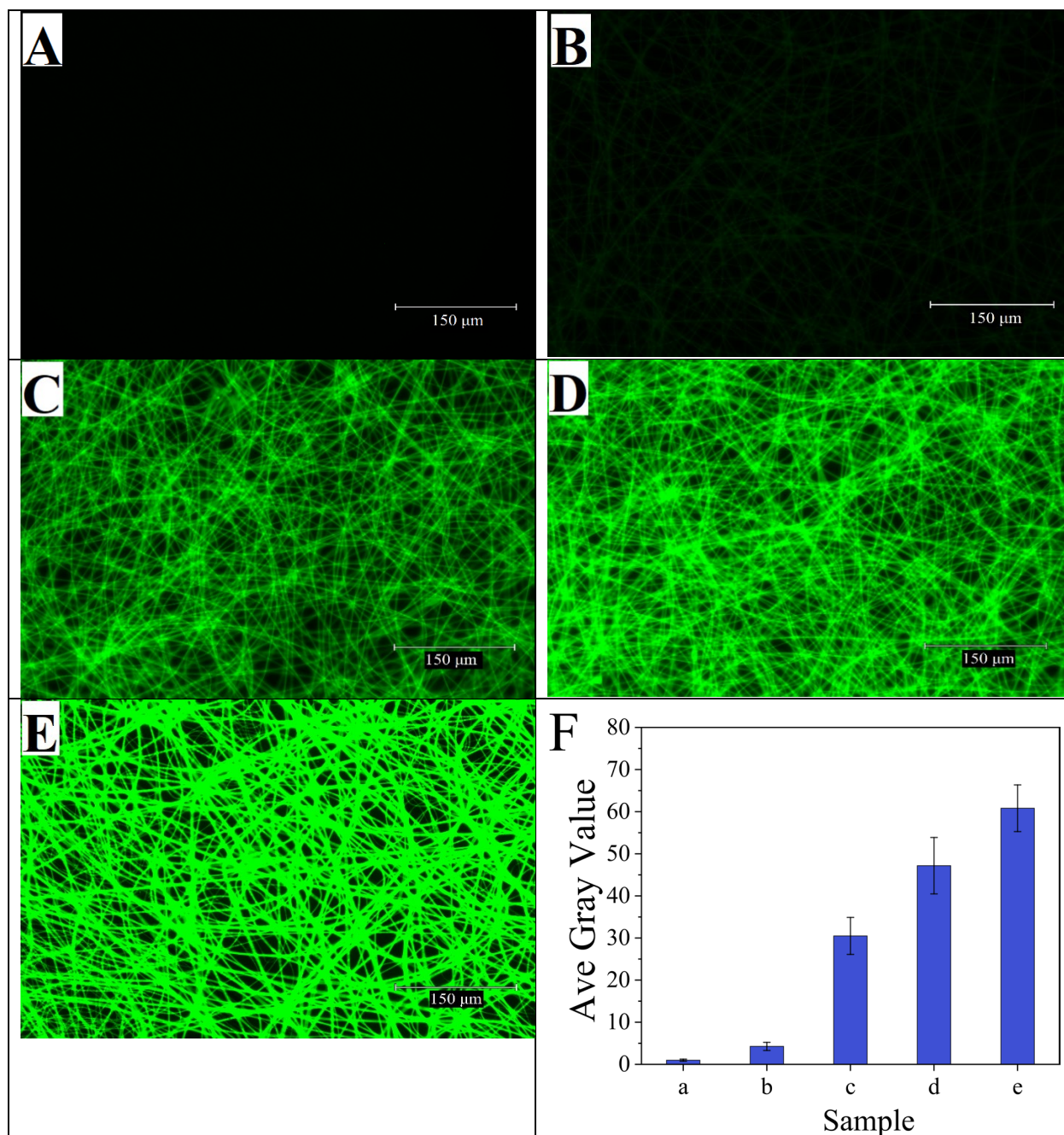
670

671

672

673

674



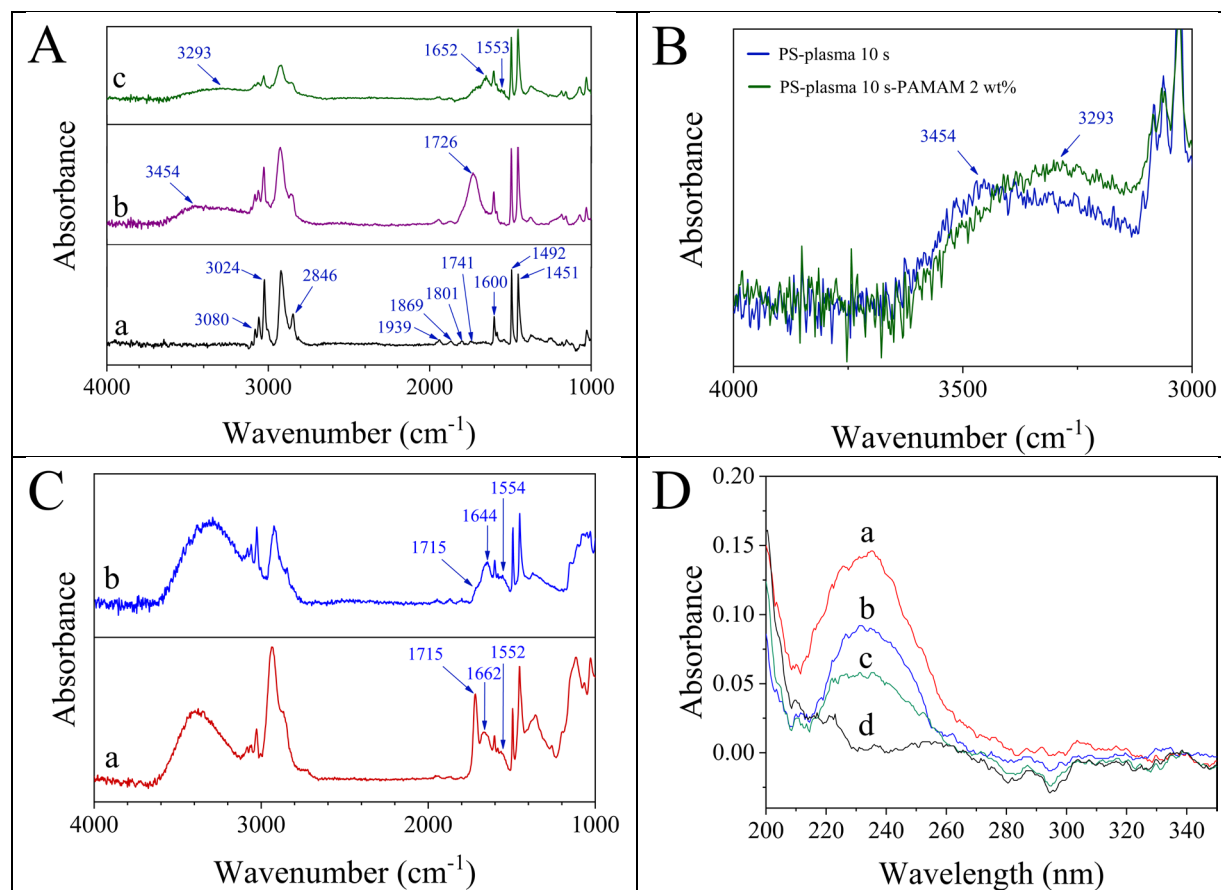
675

676 Fig. 2. Fluorescence images of A) pure PS, B) PS-plasma 10 s, C) PS-plasma 10 s-PAMAM 0.5 wt.%, D)  
 677 PS-plasma 10 s-PAMAM 1 wt.%, E) PS-plasma 10 s-PAMAM 2 wt.%, and F) quantification of  
 678 fluorescent intensity of different samples (a) pure PS, (b) PS-plasma 10 s, (c) PS-plasma 10 s-PAMAM  
 679 0.5 wt.%, (d) PS-plasma 10 s-PAMAM 1 wt.%, and (e) PS-plasma 10 s-PAMAM 2 wt.%.

680

681

682



683

684 Fig. 3. A) ATR-FTIR spectra of (a) pure PS, (b) PS-plasma 10 s, and (c) PS-plasma 10 s-PAMAM 2  
 685 wt.% ESFs, B) zoom at 3000-4000  $\text{cm}^{-1}$ , C) (a) PS-plasma 10 s-PAMAM 2 wt.%-glutaraldehyde and (b)  
 686 PS-plasma 10 s-PAMAM-2 wt.%-glutaraldehyde-anti-IL-10, and D) UV-vis spectra of unreacted  
 687 glutaraldehyde in (a) PS-plasma 10 s-PAMAM 0.5 wt.%-glutaraldehyde, (b) PS-plasma 10 s-PAMAM 1  
 688 wt.%-glutaraldehyde, (c) PS-plasma 10 s-PAMAM 2 wt.%-glutaraldehyde, and (d) pure PS.

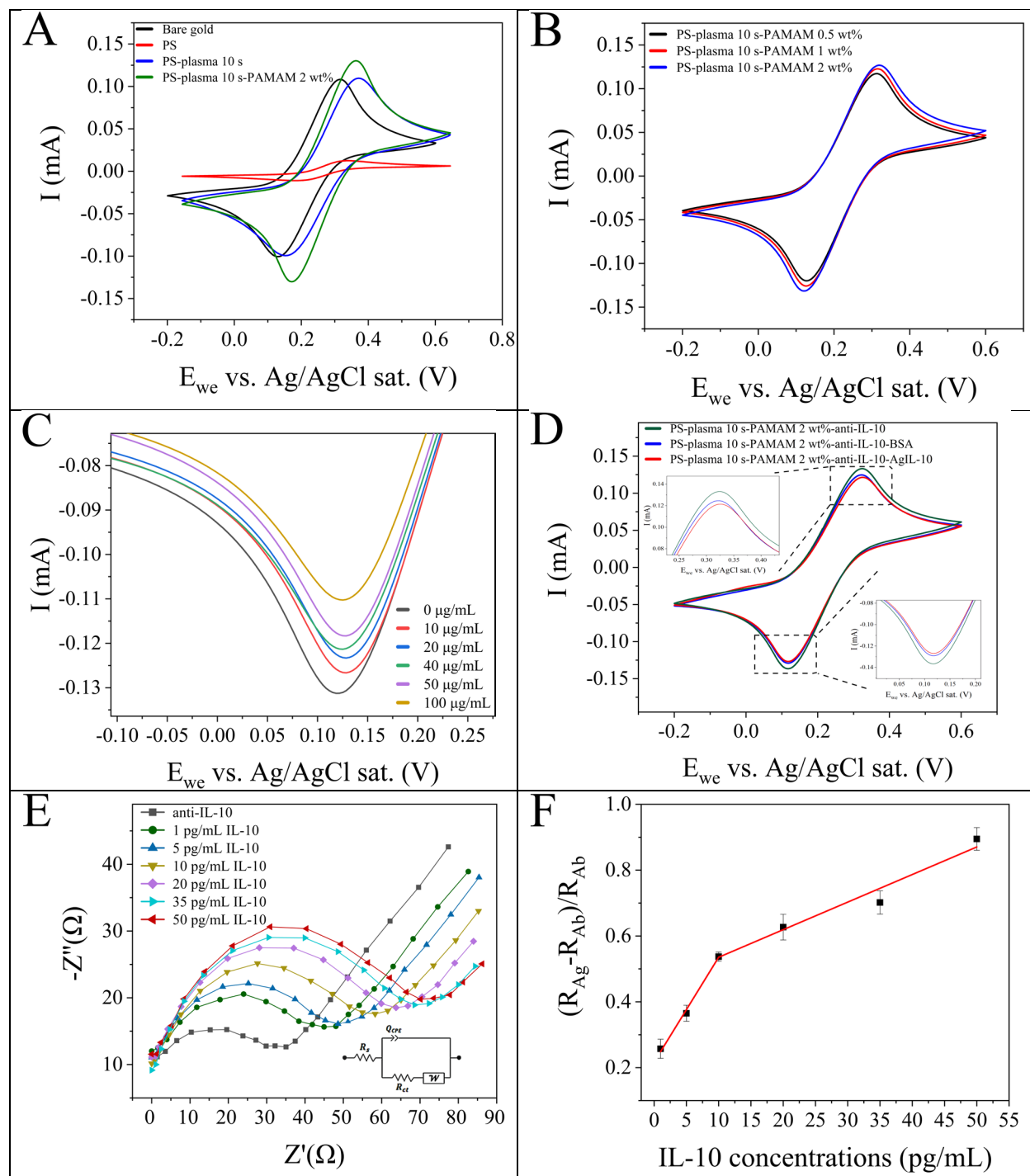
689

690

691

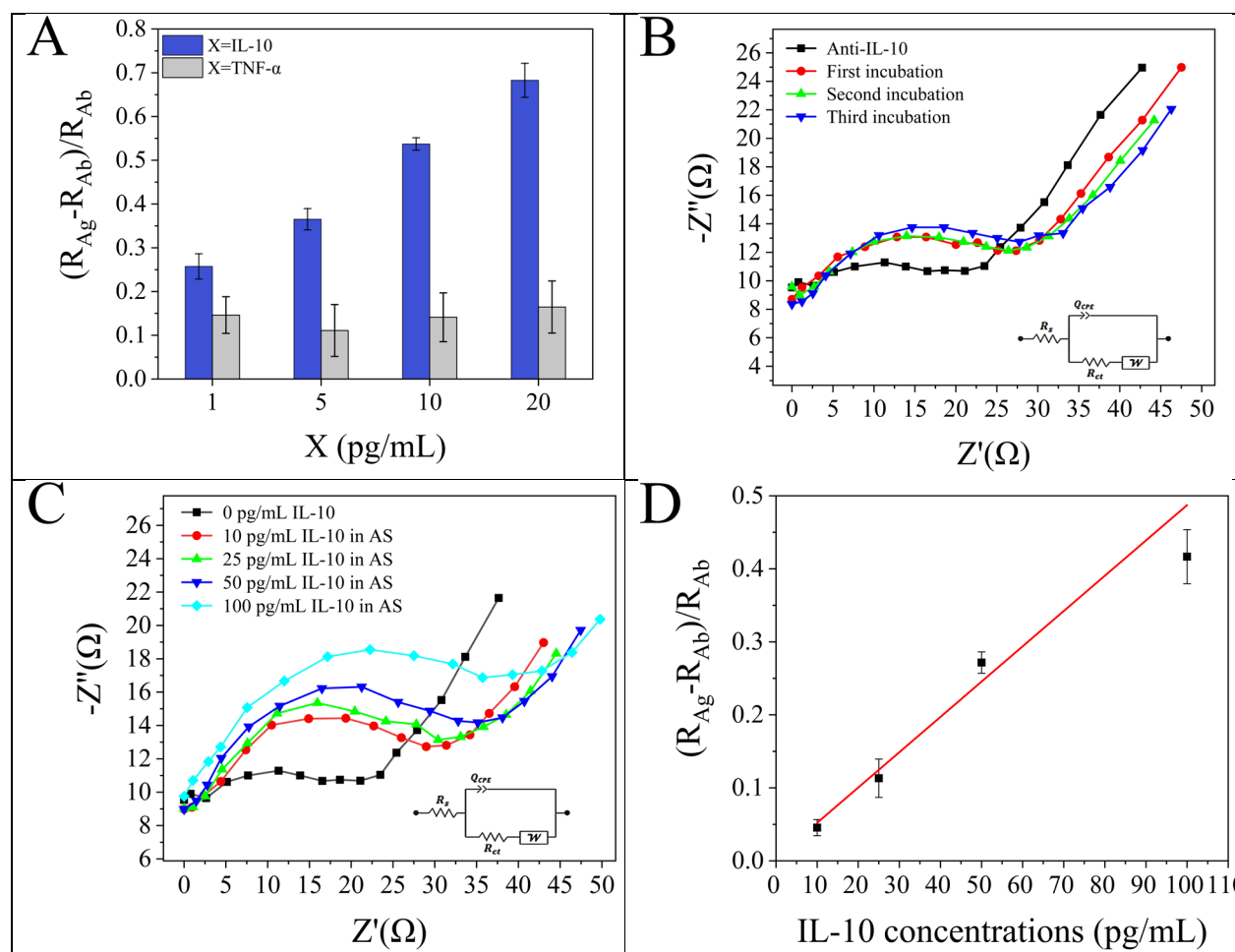
692

693



694

695 Fig. 4. A) CVs of different stages of immunosensor preparation, B) CV of PS-plasma10 s-PAMAM with  
 696 different concentrations electrode, C) effect of different immobilized anti-IL-10 concentrations (10, 20,  
 697 40, 50, and 100  $\mu\text{g/mL}$ ) on reducing the redox current, D) evaluation of anti-IL-10 activity (10  $\mu\text{g/mL}$ ) on  
 698 the fiber surface, E) Nyquist plots of PS-plasma10 s-PAMAM 2 wt.%-glutaraldehyde-anti-IL-10 ESFs  
 699 modified gold electrode of AgIL-10 detection ranging from 1 to 50 pg/mL, and F) calibration curves of  
 700 the ESFs based immunosensors for the detection of AgIL-10.



701

702 Fig. 5. A) Selectivity results of the developed immunosensors, B) Nyquist plots of three times incubation  
 703 of AS (without AgIL-10) on PS-plasma 10 s-PAMAM 2 wt.% ESFs modified gold electrode, C) Nyquist  
 704 plots of the immunosensor for AgIL-10 detection in AS, and D) detection calibration curves of the  
 705 immunosensor toward AgIL-10 in AS.

706

707

708

709

710

711

712

713

714

715  
716

Table 1. Comparison of analytical characteristics of other immunosensors reported so far for IL-10 detection with the presented ESFs based immunosensor.

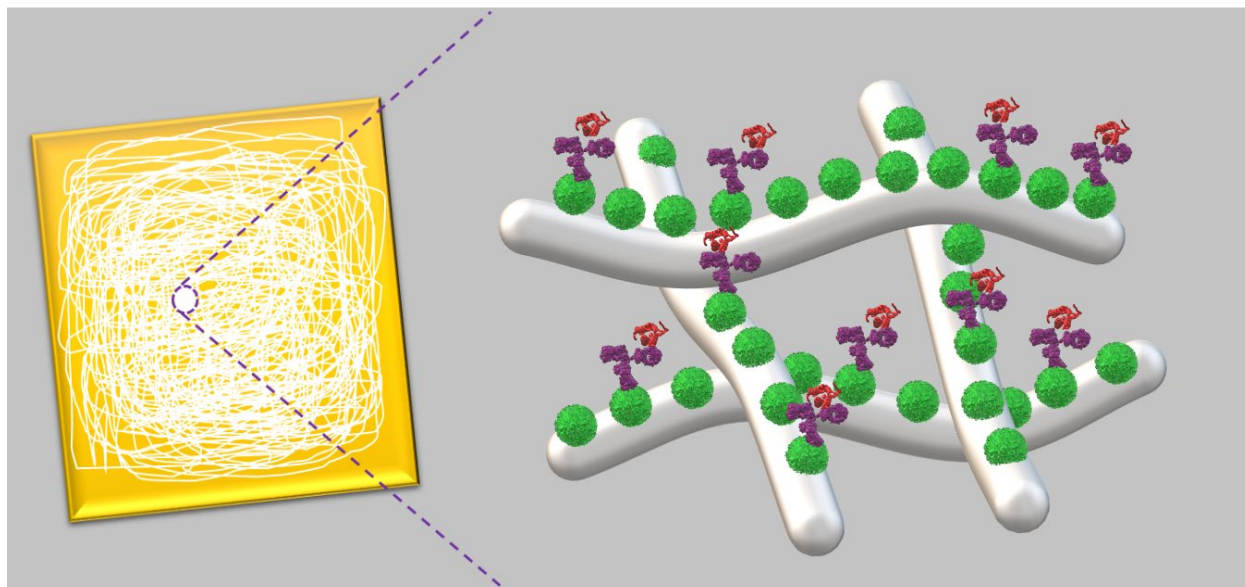
Immunosensors fundamentals	Development Method	Transduction technique	Linear Range	LOD	Ref.
Epoxy-functionalized mPDGs on a glass substrate	Immobilization	Fluorescence	0.25 µg/mL	-	[50]
HfO <sub>2</sub> grown by ALD on silicon substrate	ALD	EIS	0.1–20 pg/mL	-	[5]
Diazonium modified gold microelectrodes	Soft lithography	EIS	1–15 pg/mL	-	[51]
Polypyrrole microwires (PPy-µWs)	Soft lithography	EIS	1–50 pg/mL	0.122 pg/mL	[52]
Antibody conjugated gold nanorods	Microfluidic patterning	LSPR	5–20 pg/mL	10.97 pg/mL	[53]
MHDA modified gold microelectrodes	Soft lithography	EIS	1–15 pg/mL	-	[54]
Diazonium modified gold microelectrodes	Soft lithography	EIS	1–15 pg/mL	0.3 pg/mL	[11]
Capture-end NPs modified PTFE membrane	Conjugation	SERS	0.01-100 pg/mL	0.1 pg/mL	[55]
Gold LSPR strip	Nanoimprinting lithography	LSPR	0.2–200 nM	-	[56]
Polypyrrole modified silicon nitride (Si <sub>3</sub> N <sub>4</sub> )	Casting	EIS	1–10 pg/mL	0.347 pg/mL	[4]
Graphene interdigitated electrodes (IDEs)	Aerosol-jet-printed	EIS	0.1–2 ng/mL	46 pg/mL	[57]
One-dimensional photonic crystal (1DPC)	PIAD	BSW	250 pg/mL	110 pg/mL	[58]
PAMAM decorated plasma-treated electrospun PS fibers	Electrospinning	EIS	1–50 pg/mL	1 pg/mL	This work

717 LOD – limit of detection; mPDGs – magnetic poly (divinylbenzene-co-glycidyl methacrylate) colloidal particles; HfO<sub>2</sub> – hafnium oxide; ALD –  
718 atomic layer deposition; EIS – electrochemical impedance spectroscopy; LSPR – localized surface plasmon resonance; MHDA –  
719 mercaptohexadecanoic acid; NPs – nanoparticles; PTFE – polytetrafluoroethylene; SERS – surface-enhanced Raman spectroscopy; PIAD – plasma  
720 ion-assisted deposition technology; BSW – Bloch surface waves; PAMAM – polyamidoamine; PS – polystyrene.

721

722

723  
724  
725  
726  
727



728  
729  
730  
731  
732  
733  
734  
735  
736